Signatures of Eurasian heat waves in global Rossby wave spectra

Iana Strigunova, Richard Blender, Frank Lunkeit, and Nedjeljka Žagar

Meteorological Institute, Center for Earth System Research and Sustainability (CEN), Universität of Hamburg, Grindelberg 5, 20144 Hamburg, Germany

Correspondence: Iana Strigunova (iana.strigunova@uni-hamburg.de)

Abstract. This paper investigates systematic changes in the global atmospheric circulation statistics during Eurasian heat waves. The investigation of Rossby wave energy anomalies during heat waves is based on the time series of Hough expansion coefficients representing Rossby waves with the troposphere-barotropic structures during the extended boreal summer in the ERA5, ERA-Interim, JRA-55, and MERRA reanalyses. The climatological Rossby-wave energy distribution is shown to follow a χ^2-distribution with skewness dependent on the zonal scale.

The heuristic approach reveals signatures of Eurasian surface heat waves on global energy spectra. It is shown that the skewness in planetary waves increases during Eurasian heat waves while the opposite occurs in the zonal mean flow. No change in the skewness is found in synoptic-scale Rossby waves. Instead, synoptic zonal wavenumbers $k = 7 - 8$ are characterised by a statistically significant increase of about 5% in the intramonthly variance with respect to the climatology. The largest increase of about 20% in the intramonthly variance is found in the zonal mean state asymmetrical Rossby wave with the meridional index 6 along with the decrease in the mode 4. This reflects the weakening of the mean westerlies near their core at 45°N and their strengthening at higher latitudes around 75°N.

Keywords: Eurasian heat waves, Rossby waves, global energy spectra,circulation statistics, skewness, entropy, intramonthly variance

1 Introduction

Heat waves, periods with the daily maximum temperatures exceeding the climatological conditions by certain thresholds, have been increasing in numbers and magnitude, especially over Eurasia (e.g., Rousi et al., 2022). While the current operational numerical weather and ensemble prediction systems forecast such extremes several weeks ahead (e.g., Emerton et al., 2022), understanding the mechanism and dynamics of heat waves poses a challenge. Heat waves are connected with persistent high-pressure systems (blockings). Numerous studies focus on the onset and drivers of blocking; however, no consensus exists due to complexity of dynamical and thermodynamical processes involved (e.g., Kautz et al., 2022). Blockings are often parts of large-scale quasi-stationary wave patterns (e.g., Stefanon et al., 2012). On one side, persistent weather patterns are part of internal variability. On the other side, the effect of climate change on the frequency and persistence of these patterns is still under

debate (Woollings et al., 2018). For example, Park and Lee (2019) showed that these persistent weather patterns can be forced or triggered by remote anomalous tropical heating ("tropical forcing"). While the physical mechanisms leading to blockings are under discussion (Petoukhov et al., 2013; Nakamura and Huang, 2018; Teng and Branstator, 2019; Wirth and Polster, 2021), the quasi-stationary behaviour of these wave patterns is shown to lead to concurrent extreme events (Kornhuber et al., 2020; Fuentes-Franco et al., 2022).

In contrast to previous studies investigating particular aspects of heat waves, our research aims to identify changes in the global Rossby-wave circulation statistics during Eurasian heat waves. While a number of studies addressed particular aspects of heat waves over Eurasia (e.g., Feudale and Shukla, 2011; Schneidereit et al., 2012; Trenberth and Fasullo, 2012; Drouard and Woollings, 2018), their effects on the global spatiotemporal variance spectra have not been studied. We analyze the global three-dimensional (3D) circulation during Eurasian heat waves in terms of horizontal and vertical scales of the Rossby waves and compare it with the global circulation climatology. As we show, the probability density function (PDF) of the Rossby-wave circulation, which is described by the χ^2-distribution, changes during Eurasian heat waves. The changes are quantified by skewness and entropy measures for different zonal wavenumbers. The associated reduction of the number of active degrees of freedom compared to climatology can be used to explain the coarse structure of blocking events in the midlatitude troposphere.

The distributions of atmospheric fields are in general known to be non-Gaussian (Sura et al., 2005; Perron and Sura, 2013). However, the Central Limit Theorem may still be applicable when the sums of components in high-dimensional systems are involved, with assumptions of independent and identical distributions of summing components[1]. As we demonstrate, the distributions of anomalies in atmospheric energy can appear visually close to the normal distribution due to the Central Limit Theorem. However, the energy anomaly distributions are still skewed, which can be considered as an inherited property from energy (χ^2-distributions). The skewness, γ, of the χ^2-distribution is given by $\sqrt{8/df}$ and the excess kurtosis, κ, is given by $12/df$ with the number of independent degrees of freedom denoted df (Wilks, 2011). In the χ^2-distribution, the term "degrees of freedom" is defined by the number of sum of squares of independent (uncorrelated) normally distributed variables. In our analysis, the number of degrees of freedom is the number of all possible modes used in the projection, while the number of active degrees of freedom is a measure of the concentration of energy in large wavenumbers during a heat wave. It is important that localized structures like blocking do not consist of a finite set of low wavenumber modes but can also include contributions from higher wavenumbers (as is the case for Fourier series). Therefore, the number of active degrees of freedom is not a sharp condition but can be used to measure the system's complexity. Note that because the atmospheric circulation is the composite of the zonal mean state and the superposition of waves which might be dependent, the statistical properties might deviate from the ideal situation.

Advanced statistical methods are common tools in the research of extreme weather events. For example, Galfi and Lucarini (2021) analyzed surface heat waves using Large Deviation Theory and found that the associated persistent atmospheric patterns are not typical (in the statistical sense) compared to the climatology but follow a dynamics which is already encoded in the

[1]Under the independence of components or variables in a high-dimensional system, one can consider that its time series are uncorrelated. The identity of distributions of summing components can be regarded in terms of their mean and variances being equal.

natural climate variability. Lucarini and Gritsun (2020) considered blockings as manifestations of Unstable Periodic Orbits and their stability as an indicator of predictability and the involved number of degrees of freedom. They find low predictability at the onset and the decay, and increased predictability in the mature phase of blocking events in the Atlantic.

A more common tool for the examination of midlatitude circulation during heat waves is the Fourier series analysis of single variable data along the latitude circles. This approach identifies anomalies in the planetary- and synoptic-scale Rossby waves during extreme events in terms of the Fourier amplitudes and phases of temperature, geopotential or wind variables at different levels. For example, Screen and Simmonds (2014) found a significant increase in the monthly variance and mean of anomalies of the Fourier amplitudes of 500 hPa geopotential heights for zonal wavenumbers 3-8 and suggested that amplified planetary waves are connected with temperature and precipitation extremes. Coumou et al. (2014) analyzed wind fields at 300 and 500 hPa and found out that zonal wavenumbers $6-8$ are the most probable candidates for quasi-resonance (amplified quasi-stationary Rossby waves due to the resonance with free waves trapped within the waveguide) according to Petoukhov et al. (2013). More recently, Kornhuber et al. (2019) showed the coupling between the zonal wavenumber 7 in daily wind and temperature data at several standard pressure levels and surface extremes, such as heat waves and floods which occurred during the boreal summer 2018.

Our heuristic approach to spectral analysis of heat waves considers the horizontal and vertical scales simultaneously by using the normal-mode function (NMF) decomposition to project daily circulation fields onto Rossby and non-Rossby components (Kasahara, 2020). The NMF decomposition is multivariate meaning that the wind and geopotential variables are represented by the same spectral expansion coefficient thereby separating the circulation into the balanced (or Rossby) and unbalanced (non-Rossby) components[2].

Previous applications of the NMF decomposition showed that modal analysis complements other methods of analysing global circulation by providing scale- and dynamical regime dependent information on the variability and by quantifying it in wavenumber space (Žagar et al., 2017, 2020, 2019). Žagar et al. (2020) quantified amplitudes and trends in midlatitude traveling and quasi-stationary Rossby waves and in the equatorial wave activity in the reanalysis data. They found a statistically significant reduction of subseasonal variance in Rossby waves with zonal wavenumber $k=6$ along with an increase in variance in wavenumbers $k=3^{\backsim}5$ in the summer seasons of both hemispheres. However, they did not attempt to relate these changes with the surface weather or extreme events. This task is carried out in the present study.

Our goal is to investigate whether and how surface heat waves during boreal summer over Eurasia affect the global atmospheric variability spectrum. While it is not evident *a priori* that regional heat waves have their signatures in the global Rossby wave spectra, we show that this is, in fact, the case. First, we demonstrate statistically significant changes in the global total energy anomalies PDFs during heat waves. Then, we interpret the dynamics of the planetary Rossby waves through the change in active degrees of freedom and show its relation with the entropy reduction during Eurasian heat waves.

The paper is organized as follows. The 3D decomposition method, statistical analysis and the heat waves identification algorithm are explained in Section 2. Section 3 contains results. First, we present examples of the NMF decomposition for two

[2]The real-time decomposition of the ECMWF circulation in Rossby and non-Rossby components is available on the MODES webpage https://modes.cen.uni-hamburg.de.

recent heat waves. This is followed by the results of statistical analysis of spatial spectra (climatological and heat waves energies) and its interpretation by filtering parts of balanced circulation back to physical space. Finally, we discuss how temporal variance spectra change during heat waves. Conclusions are presented in Section 4.

2 Method and Data

In this section we describe our research method that makes use of the NMF decomposition and the MODES software (Žagar et al., 2015). The method is applied to the four modern reanalysis datasets. We present the criteria for Eurasian surface heat waves and associated selection method for the spectral expansion coefficients.

2.1 Normal-mode function decomposition of global circulation

The NMF decomposition is carried out in the terrain-following, global coordinate system $(\lambda, \varphi, \sigma)$, where σ is the ratio of the vertical level pressure and the surface pressure, λ denotes longitude and φ is latitude. At every time step t, the horizontal winds (u, v) and geopotential height (h) on σ levels are projected to precomputed vertical and horizontal structure functions (VSFs and HSFs, respectively). The VSFs are the numerical solutions of the vertical structure equation whereas the HSFs are eigensolutions of the Laplace equation without forcing and are given in terms of the Hough harmonics. The Hough harmonics are defined as a product of the latitude-dependent Hough functions and harmonic waves in the longitudinal direction. The horizontal and vertical structures are coupled by the eigenvalues of the vertical structure equation, the so-called "equivalent depth" which is also the mean depth of the linearized shallow-water equations. The reader is referred to Žagar et al. (2015) and Kasahara (2020) and references therein for details of the theory.

MODES is applied to the four modern reanalyses: ERA5 (Hersbach et al., 2020), ERA-Interim (Dee et al., 2011), the Japanese 55-year Reanalysis JRA-55 (Kobayashi et al., 2015), and the Modern-Era Retrospective analysis for Research and Applications MERRA (Rienecker et al., 2011). We use daily data at 12 UTC from 1980-2014 (1980-2019 for ERA5) on the regular Gaussian grid that consists of 256×128 grid points in the zonal and meridional directions, respectively. Vertically the data are interpolated on the predefined 43 σ levels.

The projection consists of two steps. In the first step, the 3D data $\mathbf{X}(\lambda, \varphi, \sigma)$ is expanded into a series of orthogonal VSFs G_m according to

$$\mathbf{X}(\lambda, \varphi, \sigma) = (u, v, h)^{\mathrm{T}} = \sum_{m=1}^{M} G_m(\sigma)\, \mathbf{S}_m\, \mathbf{X}_m(\lambda, \varphi)\ . \tag{1}$$

The vertical mode index m ranges from 1 to M, the total number of vertical modes, that can be equal or less the number of vertical levels. For every m, the nondimensional data matrix $\mathbf{X}_m(\lambda, \varphi) = (\tilde{u}, \tilde{v}, \tilde{h})^T$ is obtained by the normalisation by the 3×3 diagonal matrix $\mathbf{S}_m$ with elements $\sqrt{gD_m}$, $\sqrt{gD_m}$, D_m, where D_m denotes the equivalent depth of the vertical mode m. The nondimensional variables are defined with $\tilde{}$.

In the second step, the horizontal nondimensional motions are projected onto a series of Hough harmonics $\mathbf{H}_n^k$ for every m as

$$\mathbf{X}_m(\lambda,\varphi) = \sum_{n=1}^{R} \sum_{k=-K}^{K} \chi_n^k(m)\, \mathbf{H}_n^k(\lambda,\varphi;m)\,, \tag{2}$$

where K denotes the total number of zonal waves and R is the total number of meridional modes. The complex Hough expansion coefficients $\chi_n^k(m)$ depend on three indices: m, meridional mode index n and zonal wavenumber k. For every n, the projection includes two types of motions: Rossby modes[3] (quasi-geostrophic or balanced dynamics) and inertia-gravity modes that represent divergence-dominated unbalanced dynamics. The inertia-gravity modes consist of eastward- and westward-propagating solutions and together with the equatorial Kelvin and mixed Rossby-gravity waves constitute the non-Rossby modes that are not used in this study.

It is the inverse of Eq. (1) and Eq. (2) that is solved in the forward projection. The second step gives the complex Hough expansion coefficients $\chi_n^k(m)$ as

$$\chi_n^k(m) = \frac{1}{2\pi} \int_0^{2\pi} \int_{-1}^{1} \mathbf{X}_m(\lambda,\varphi)\, [\mathbf{H}_n^k]^* \mathrm{d}\mu\, \mathrm{d}\lambda\,. \tag{3}$$

The integration in the zonal direction is calculated by the fast Fourier transform and in meridional direction by the Gaussian quadrature.

The projection is carried out using the following truncations: $K = 100$, $M = 27$, and $R = 150$ which combines 50 meridional modes for the Rossby modes, for the eastward inertia-gravity and for westward inertia-gravity waves modes. Since the mixed Rossby-gravity mode is counted as the first balanced modes, we have 49 Rossby modes for every m and k, so that the meridional mode index goes from $n = 1$ to $n = 49$.

We are interested in the balanced circulation with the troposphere-barotropic vertical structure that characterises the midlatitude weather during heat waves. As shown in Fig. 1, the first five VSFs do not change their signs below the tropopause (taken at 250 hPa), and can therefore be regarded as troposphere-barotropic modes.

2.2 Heat Waves

We analyze heat waves for the Eurasian region limited by the Ural mountains [35°N-65°N, 10°W-60°E]. The study area is frequently affected by heat waves (e.g., Zhou and Wu, 2016), in particular, Eastern Europe and Western Russia, a region of one of the strongest heat waves observed in recent decades (e.g., Barriopedro et al., 2011). For heat wave identification, we analyze daily 2 m temperature fields for the extended boreal summer (MJJAS) from 1980-2014 (until 2019 for ERA5). The identification algorithm applied by Ma and Franzke (2021) uses the following two criteria: (i) the temperature exceeds the 95th percentile threshold and (ii) the duration of the exceedance is larger than three consecutive time steps. As the identification algorithm is performed for each reanalysis, it is expected to have discrepancies among them. Table 1 presents the list of days with heat waves in reanalysis datasets, which is based on the algorithm mentioned above.

[3]We use both 'modes' and 'waves' interchangeably but the latter refers to the case without the zonal mean state ($k = 0$).

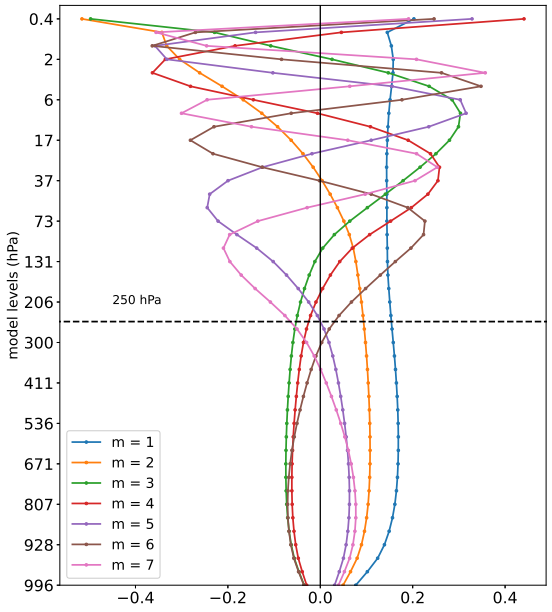

Figure 1. Vertical structure functions (VSFs) for the first seven vertical modes. VSFs are derived for 43 σ levels using the stability profile of ERA-Interim data. VSFs that do not change the sign below the tropopause (defined as 250 hPa level) are troposphere-barotropic modes.

2.3 Time series of Rossby wave energy anomalies

The total (kinetic plus available potential) energy of a single mode $\nu = (k, n, m)$ is given by the square of the absolute value of the Hough coefficient (i.e. in terms of its real and imaginary parts) as

$$I_\nu = I_n^k(m) = \frac{1}{2} g D_m \left| \chi_n^k(m) \right|^2 , \tag{4}$$

where g is the gravity. See Kasahara (2020) for the derivation of Eq. (4).

The time series of the daily total energy is denoted $I_\nu(t)$ span over the period of extended boreal summer (MJJAS, May-September) within 35 years (1980-2014) for ERA-Interim, JRA-55, MERRA ($N_y = 35$) and 40 years (1980-2019) for ERA5 ($N_y = 40$). The climatological annual cycle is obtained as an average over all years (N_y) for each day in MJJAS as

$$\langle I_\nu \rangle = \frac{1}{N_y} \sum_{y=1}^{N_y} I_{\nu,y} , \tag{5}$$

and subtracted from daily energies to compute the energy deviations (or anomalies) as

$$I'_\nu = I_\nu - \langle I_\nu \rangle . \tag{6}$$

Table 1. Heat waves in Eurasia during May-September 1980-2019

		ERA5	ERA-Interim	JRA-55	MERRA
	Start date	Number of detected days			
1	1994-09-23	3	3	2	3
2	2006-06-18	12	10	12	10
3	2006-09-20	3	5	6	2
4	2007-05-20	12	12	12	12
5	2007-08-21	6	6	6	6
6	2008-09-05	4	3	4	3
7	2010-06-28	26	27	27	26
8	2010-07-27	21	21	19	21
9	2012-05-09	4	4	4	4
10	2012-06-14	4	3	4	3
11	2013-05-02	7	7	6	5
12	2014-05-17	5	3	3	3
13	2014-06-05	5	6	5	6
14	2015-06-02	3	-	-	-
15	2015-08-11	3	-	-	-
16	2015-09-17	11	-	-	-
17	2016-06-21	4	-	-	-
18	2016-08-20	9	-	-	-
19	2018-05-02	8	-	-	-
20	2018-06-27	4	-	-	-
21	2018-07-13	22	-	-	-
22	2018-08-29	7	-	-	-
23	2018-09-11	12	-	-	-
24	2019-06-01	3	-	-	-
25	2019-06-08	5	-	-	-
26	2019-06-18	3	-	-	-
27	2019-06-23	4	-	-	-
28	2019-07-24	3	-	-	-
$\sum$days		213	110	110	104

The time series of I'_ν define the climatology.

At this stage, we form also the time series of energy anomalies with time steps of the observed heat waves according to Table 1. Although only 13 heat waves are identified in ERA-Interim, JRA-55 and MERRA due to the shorter datasets, we include

them to increase the sample size. We note that all 13 heat waves are identified in all reanalyses, but the individual datasets differ, as can be inferred from the number of detected days. Thus, we consider them as different realizations. We normalize energy anomalies by their climatological standard deviation σ_ν

$$\tilde{I}'_\nu = \frac{I'_\nu}{\sigma_\nu} \, . \tag{7}$$

The mode-wise normalisation by the standard deviation is crucial since the energy spectrum is red not only in terms of the horizontal scales (Žagar et al., 2017), but also the vertical scale. Note that the entire time series of energy anomalies (climatology) and time series during heat waves are normalized by different σ. This procedure is applied for every reanalysis dataset independently.

The next step is to split the normalized energy anomalies of the single Rossby modes into planetary ($k = 1-3$) and synoptic ($k = 4-10$) intervals, and then to average over the troposphere-barotropic modes $m = 1-5$ within these intervals. The mean zonal flow is given by $k = 0$. For each k, averaging is applied also over meridional modes whenever the results are discussed in terms of a single modal index.

Finally, we combine the time series of normalized energy anomalies in the above-mentioned wavenumber ranges. Žagar et al. (2020) showed that the differences between climatological energy spectra for the four reanalyses are minor. Therefore, our PDFs consist of independent but similar time series. Thus, we can detect robust features of distributions of energy anomalies across different datasets.

3 Results

First, Fig. 2 demonstrates that the global energy in a single Rossby mode is χ^2-distributed. The presented example uses the energy (Eq. 4) of the Rossby mode with $(k,n,m) = (7,3,1)$ which is associated with variability in midlatitude barotropic circulation. The histogram and the fit of the χ^2-distribution with two degrees of freedom, $df = 2$, correspond to the real and the imaginary parts of the time series of $I_n^k(m) = I_3^7(1)$. The Kolmogorov-Smirnov test reveals a negligible p-value, confirming the fit. Therefore, we find that approximation of χ^2-distributed energy is satisfied to a high degree, as expected.

3.1 Northern Hemisphere midlatitude circulation during heat waves

In this section, we demonstrate that the selected subset of vertical modes is suitable for the statistical analysis by demonstrating the climatological circulation and two selected heat wave events with applied filtering. We show the ERA5 results, but other datasets provide similar results. Figure 3a depicts the May-September balanced circulation (Rossby modes with $k > 0$ and all m, n) at a single σ level close to 500 hPa. The pattern remains almost the same when we restrict vertical modes to only the troposphere-barotropic modes, $m = 1-5$ (Fig. 3b). This confirms that our selection of modes is suitable for analyzing the troposphere-barotropic circulation, i.e. the patterns observed during surface extreme events commonly associated with the blocking.

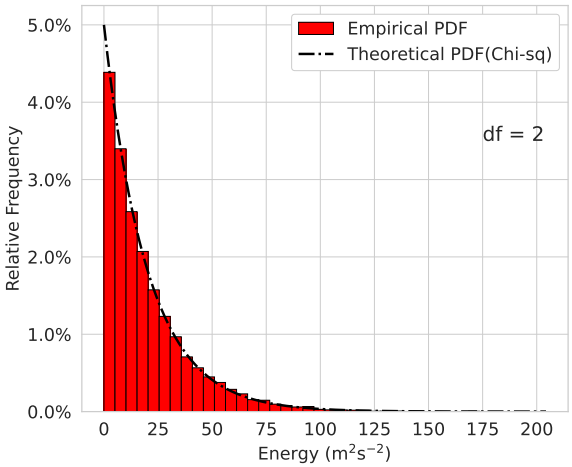

Figure 2. Atmospheric energy (empirical) distribution in the Rossby wave with zonal wavenumber $k = 7$, meridional mode $n = 3$ and vertical index $m = 1$ for 1980-2014. The dashed black lines correspond to the theoretical (χ^2) distribution (df are the degrees of freedom).

This structure is clearly recognized when we reconstruct circulation during two recent extreme heat events: the Russian Heat Wave in 2010 (Barriopedro et al., 2011) and the European Heat Wave in 2019 (Xu et al., 2020). The difference with respect to climatology which is presented in Fig. 3b. In both cases, we observe strong positive anomalies over the locations of the observed surface extremes (Western Russia and Europe) with nearby negative anomalies. For the Russian Heat Wave in Fig. 3c, d, the anomalies over Central and Southern Asia reveal cyclones which have produced extreme rainfall known as the Pakistan Flood (Lau and Kim, 2012). Furthermore, the wavy pattern along the latitudinal belt depicts teleconnections (Teng and Branstator, 2019). The plots with the difference between climatology and each heat wave (Fig. 3d,f) demonstrate the meridional extension of the waves from polar to tropical regions confirming the impact of these regions on midlatitude extremes (Behera et al., 2012). While the patterns shown in Fig. 3 are qualitatively known from previous studies, our result was obtained by a novel method that allows a scale-dependent quantification of the associated circulation with respect to the global climatology. This result also justifies our use of the subset of vertical modes in the statistical analysis presented below.

3.2 Statistics in modal space

The example in the previous section demonstrated how the Rossby circulation is altered regionally during Eurasian heat waves. Our next step is to investigate how these heat waves affect (if) the global spatial variability spectrum, i.e. their impact on global circulation. Here, the term global variability spectrum refers to the PDFs of the normalized anomalies in global energy, and the effects (or signatures) of heat waves implies significant changes in the distribution of energy anomalies. As a first step, we analyze the climatological PDFs in terms of zonal wavenumbers corresponding to three ranges as described in Section 2: (i) the

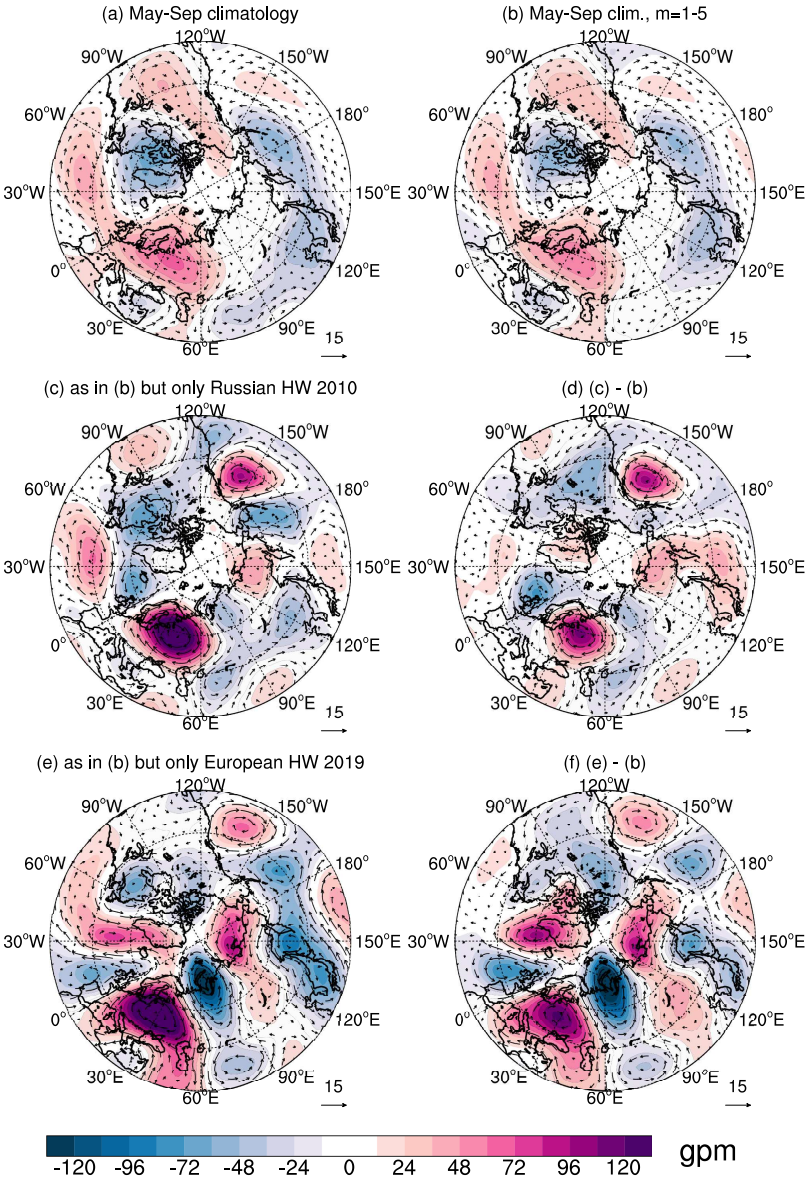

Figure 3. Climatological Rossby wave circulation for extended boreal summer (MJJAS) at σ level close to 500 hPa (ERA5 model level 30) in the midlatitudes (35°N - 65°N). Coloured contours are geopotential height anomalies (in gpm) for Rossby waves and (a) zonal wavenumbers $k > 0$ (no zonal mean state), all meridional modes n and all vertical modes m. (b) as in (a), but only troposphere-barotropic vertical modes, $m = 1 - 5$, (c) as in (b) but for the Russian Heat Wave (HW) in 2010. (d) Difference between the (c) and (b). As in (c), (e, f) illustrate Rossby waves during the European Heat Wave (HW) 2019. Wind speed is shown by the length of the wind vectors (15 $\mathrm{m/s^{-1}}$ as a reference vector).

zonal mean state, $k = 0$, (ii) the planetary-scale circulation $k = 1 - 3$, and (iii) the synoptic-scale circulation with $k = 4 - 10$. We focus on the skewness which is not impacted by the normalization.

Figure 4a shows the PDF with all zonal wavenumbers included in the analysis. With the skewness equal to 0.38, the PDF clearly deviates from a Gaussian distribution. The planetary-scale (Fig. 4c) and the synoptic-scale (Fig. 4d) PDFs also do not
215 follow a normal distribution, but exhibit noticeable asymmetry, with the planetary-scale skewness almost twice greater than the one of the synoptic-scale Rossby waves.

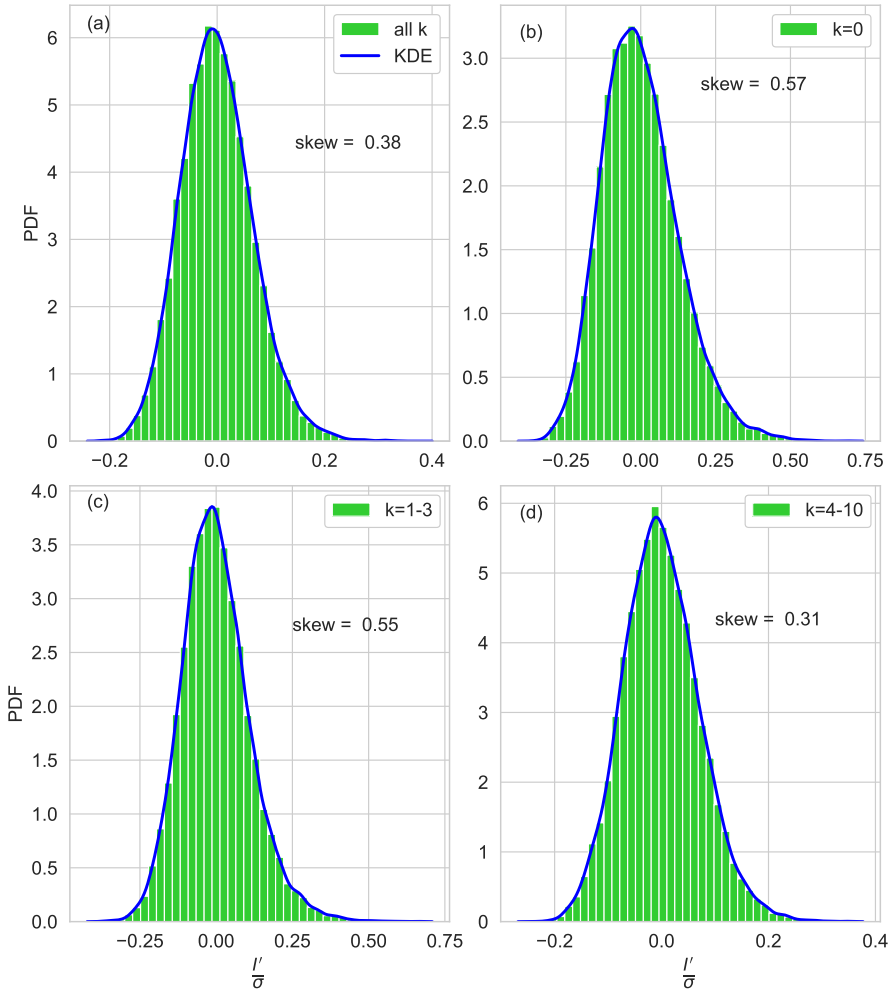

Figure 4. PDFs of normalized total energy anomalies (all k), (b) the zonal mean state ($k = 0$), (c) planetary-scale waves ($k = 1 - 3$), (d) synoptic-scale waves ($k = 4 - 10$). Empirical PDFs are depicted as green bars for extended boreal summer (MJJAS) 1980-2014 (1980-2019 for ERA5). The blue curve is the Kernel Density Estimator (KDE).

The skewness of the PDFs in Fig. 4 is based on the four reanalyses (ERA5, ERA-I, JRA-55, MERRA) combined. We apply bootstrapping with a replacement for different wavenumber ranges for a more robust statistical analysis (Fig. 5). Note that all values from reanalysis datasets are within the defined 95% confidence intervals (CI) for each wavenumber range (here is not shown). The bootstrapped skewness shows that the normalized energy anomaly distribution has the highest asymmetry in the planetary scales and zonal mean circulation which is also detected as stretched right tails in the PDFs. The different number of single modes can partly explain the different skewnesses in the four wavenumber ranges. However, changes in the dynamics can modify the skewness and the active degrees of freedom, which is addressed in the next section.

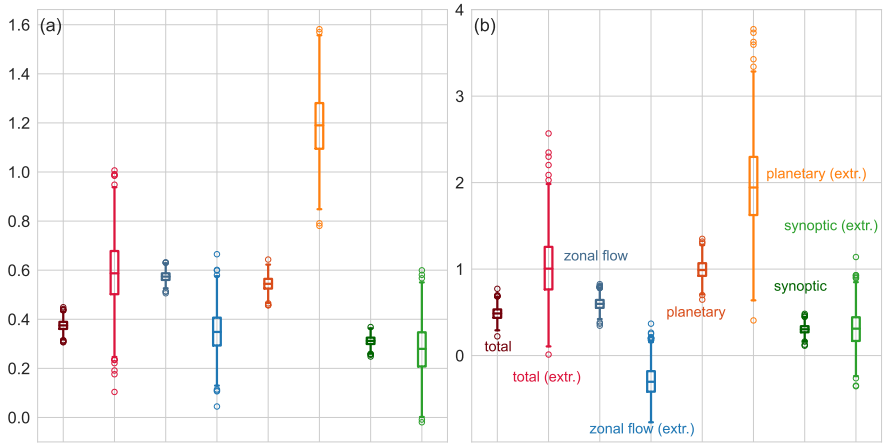

Figure 5. Box-plots for (a) skewness and (b) excess kurtosis of normalized energy anomalies distributions for four considered atmospheric components: total Rossby regime with dark- and light-red bars, the zonal mean flow as dark- and light-blue bars, planetary waves as orange and yellow, and the synoptic circulation as dark- and light-green 95%-confidence intervals are obtained through bootstrapping with replacement with 1000 simulations.

3.2.1 Surface extremes and energy statistics

Now we compare PDFs during observed heat waves over Eurasia with climatology for different parts of wavenumber space. For comparison, we consider two statistical moments, skewness and excess kurtosis, to diagnose the changes in shape, especially in the tails of distributions for the four reanalyses datasets. We find that only the difference in the skewness of the planetary-scale distribution is statistically significant, i.e the bootstrapped values are outside CIs of climatological bootstrapped skewness only during extremes.

The PDFs of the normalized energy anomalies depicted in Fig. 6 demonstrate how probabilities of the energy deviations change during surface extreme events. First, there is a positive shift in the mean except for $k = 0$, and, as a consequence, an increased probability of intermediate positive deviations.

According to Fig. 5a, the change in the skewness, which is considered as the main indicator, is the largest for the planetary-scale circulation. The excess kurtosis for extreme events is approximately twice larger than climatology (Fig. 5b), which reflects

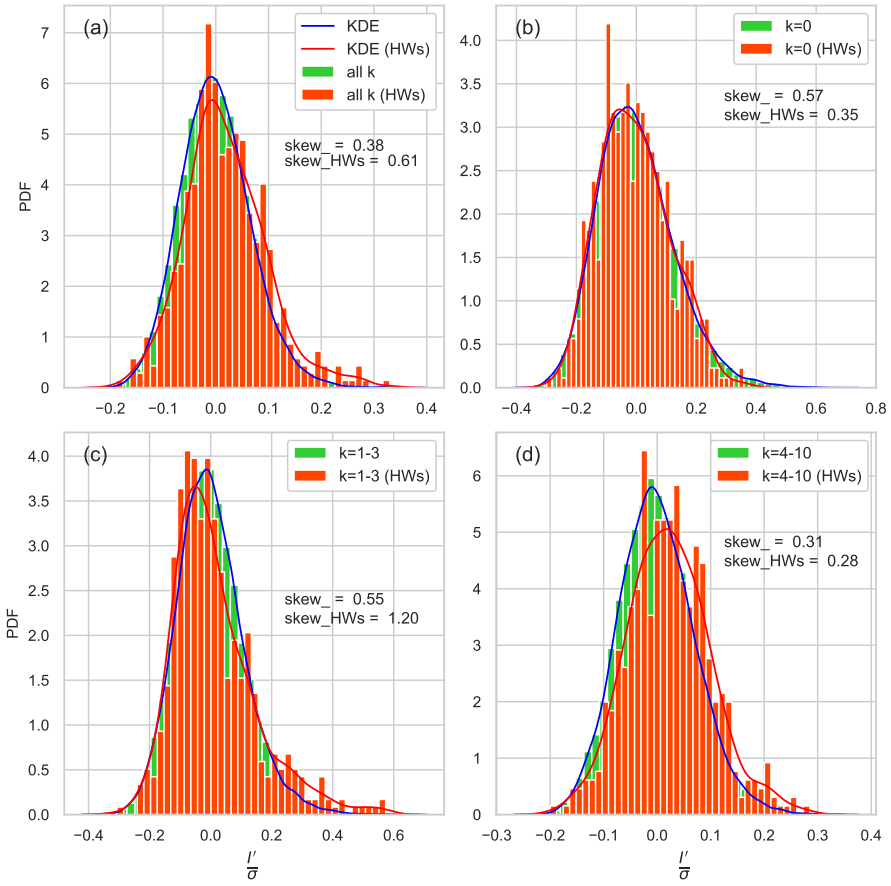

Figure 6. The same as in Fig. 4 but with normalized energy anomalies only during heat waves (HWs) presented in Table 1.

a drastic rise in the probability of extreme values. The opposite change is found for the zonal mean flow during surface heat waves, where skewness and the excess kurtosis decrease; this implies that the distribution becomes flatter with thinner tails and is less extreme. Based on this, we conclude that the amplitudes of the planetary circulation amplify as shown in Fig. 3d, f, while the zonal mean flow anomalies become weaker in agreement with Coumou et al. (2014). Thus, we have evidence that signatures of heat waves are seen in different parts of the global variability spectrum via statistically significant changes in skewness.

The increase in skewness allows for the estimation of the reduction of the active degrees of freedom during the heat waves compared to the climatological mean. For the estimation, we use the exact relation for the skewness of χ^2-distributed variable, $\gamma = \sqrt{8/df}$, where df is the number of squares of the independent Gaussian variables with a unit variance which defines the χ^2-distributed variable.

We use the ratio $df_e/df_c = \gamma_c^2/\gamma_e^2$ which says that the ratio between the number of active degrees of freedom during heat waves and climatology, df_e and df_c, is equal to the ratio of their skewnesses γ_e and γ_c, respectively. The rough estimates

$\gamma_e \approx 1.2$ and $\gamma_c \approx 0.6$, based on Fig. 5a, yield a reduction of the active degrees of freedom of the order of $df_e/df_c \approx 1/4$ during the extreme events.

Unlike the change in skewness in the PDFs of the planetary Rossby waves, there is a statistically significant change (according to the Mann-Whitney U test with 95%-confidence) in the entire PDFs of synoptic Rossby waves. The change can be seen in a distribution shift toward positive energy anomalies (figure not shown), which can be interpreted as more energy is expected at synoptic scales during heat waves. More intensive cyclones and anticyclones are found to maintain blocking throughout eddy straining (Shutts, 1983) and selective absorption (Yamazaki and Itoh, 2013) mechanisms.

Finally, we make a note on the fact that the changes in PDFs during the Eurasian heat waves apply to the global atmosphere. Our Rossby modes consist of symmetrical (n odd) and asymmetrical (n even) components with symmetry with respect to the equator defined for the geopotential height and zonal wind fields. We checked that both symmetrical and asymmetrical parts contribute to the PDFs of all meridional modes. In other words, the Rossby waves in the Southern Hemisphere might have contributed to the results presented. However, taking into account the lower frequency of atmospheric blocking (Wiedenmann et al., 2002) in the Southern Hemisphere, we may assume that this influence is negligible.

3.3 Changes in the midlatitude barotropic circulation during heat waves

The next step is to relate the PDFs of energy anomalies in large-scale circulation with physical space. This is achieved by filtering the analyzed Rossby modes ($k = 1-3, n = 1-49, m = 1-5$) to physical space, similar to what has been done in Fig. 3. Instead of case studies, now we present the circulation averaged over all days with observed extremes. As earlier, we show the horizontal circulation at ERA5 σ-level near 500 hPa as representative for the troposphere-barotropic circulation.

Figures 7b and c reveal an enhancement of positive height anomalies in the eastern part of the Baltic Sea and negative anomalies over the North Atlantic. Moreover, one can notice a north-westward shift of negative anomalies in the Asian part compared to climatology presented in Fig. 7a and the formation of positive anomalies over Chukotka and Alaska. According to Fig. 7c, the dominant patterns are zonal wavenumber 2 and 3.

Figures 7d,e show the vertical profile for $54°\mathrm{N}$ of the meridional wind speed and the geopotential height anomalies for climatology, during heat waves. Figure 7f depicts the difference between two profiles. We illustrate again that the structure is barotropic over the entire troposphere and lower stratosphere, as was observed in some studies. Moreover, there is an enhancement of northward winds over Europe ($0°\mathrm{E}-30°\mathrm{E}$) and southward winds over the Asian part of Russia ($60°\mathrm{E}-90°\mathrm{E}$) with southerlies over the Kamchatka Peninsula (Fig. 7f). Overall, we find an increase in wave amplitudes, and change in phases as can be noticed by west- and northward shifts in Fig. 7b, c and Fig. 7d, e in the Baikal lake area ($90°E - 120°E$). According to Teng and Branstator (2012) and Ragone and Bouchet (2021), the wave-3 pattern is dominant for heat waves that occurred in the US, France and Scandinavia. Therefore, the results demonstrate how atmospheric circulation is changed during surface extremes not only locally but also in remote regions, similar to the idea of teleconnection patterns noted in recent studies (e.g., Kornhuber et al., 2019).

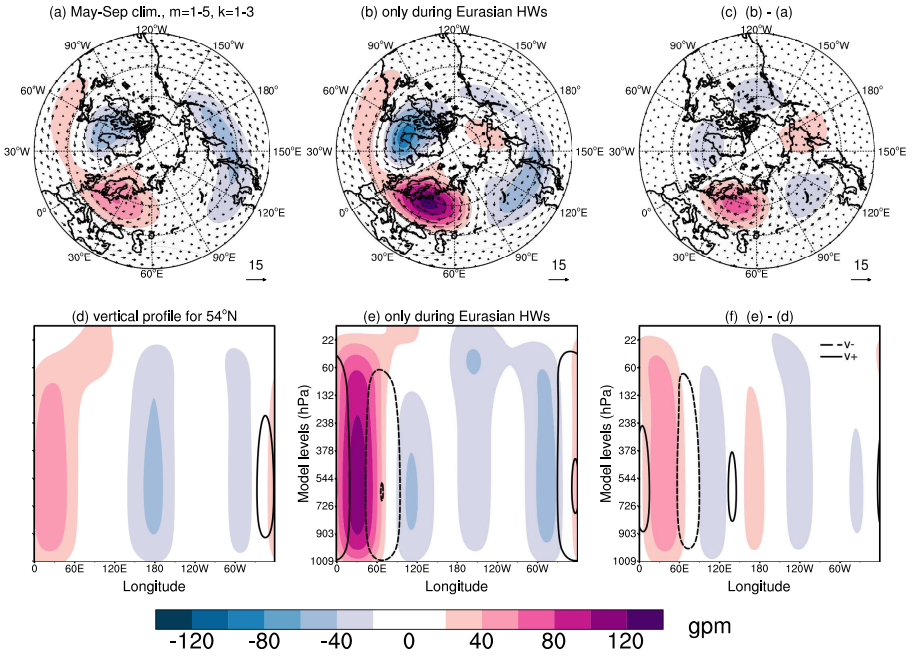

Figure 7. Planetary-scale, troposphere-barotropic Rossby waves ($k = 1 - 3$, $m = 1 - 5$, all n) at the $\sigma-$level close to 500 hPa in ERA5. Coloured contours are geopotential height anomalies, every 20 gpm. The wind speed is shown by the arrow length. (a) Mean circulation in May-September obtained in the 40-year climatology (1980-2019), (b) composite of 28 Eurasian Heat Waves (HWs) presented in Table 1, (c) difference between (b) and (a). (d) Climatological geopotential height perturbations (coloured isolines) in planetary scales along 54°N, (e) As in (d) but during HWs, (f) difference between (d) and (e). Solid and dashed contours in (d)-(f) show the planetary-scale meridional winds (northward and southward, respectively) every 2 ms^{-1}.

3.4 Intramonthly variance and entropy reduction during the heat waves

So far, we showed signatures of heat waves in spatial variance (energy). Now we look at changes in temporal variance due to extremes and couple it to the changes in entropy which measures the average uncertainty with which one knows the state of the system. The temporal variance and its square root, variability, are usually studied locally or using the time series of atmospheric indices such as North Atlantic Oscillation. The global intraseasonal variance in the reanalysis data was analyzed by Žagar et al. (2020) who showed statistically significant trends in both midlatitude Rossby waves and large-scale equatorial waves. Here, we focus on intramonthly scales associated with heat waves with the unbiased variance (Jkg^{-1}) computed as

$$V_\nu = \frac{1}{N-1}\sum_{t=1}^{N} gD_m|\chi_\nu(t) - \overline{\chi}_\nu|^2\,, \tag{8}$$

where $\overline{\chi}_\nu$ is the monthly mean and N is the number of days in a single month. As the 3D NMF expansion is a complete representation of the system, the components ν of the state vector are statistically independent and correspond to independent

degrees of freedom, as discussed in Section 2. The relative change in variance during heat waves is thus

$$\frac{\left(V_\nu - V_\nu^h\right)}{V_\nu} \quad \text{or} \quad 1 - \frac{V_\nu^h}{V_\nu}\,, \tag{9}$$

where V_ν^h is the intramonthly variance during the heat waves. To obtain the mean state, variances are averaged over months May to September and years 1980 to 2019 in ERA5. For extremes, we consider intramonthly variances for months with observed heat waves. Zonal wavenumber variance spectra of V_ν and V_ν^h are obtained by summing over the five barotropic vertical modes and over all meridional indices of the Rossby waves.

The entropy, $\mathcal{H}$, which measures the average uncertainty of the system, is defined as

$$\mathcal{H}(\mathcal{P}) = \int\limits_{R^n} \mathcal{P}(\mathbf{x}) \ln(\mathcal{P}(\mathbf{x}))\, \mathrm{d}\mathbf{x}\,, \tag{10}$$

where probability density $\mathcal{P}(\mathbf{x})$ represents the uncertainty of the state $\mathbf{x}$ of the system. The change in entropy can be described by the difference in entropy between the heat wave and climatological probability densities that are represented by diagonal matrices $\mathbf{Q}^{\mathrm{h}}$ and $\mathbf{Q}$ with entries equal to V_ν^h and V_ν, respectively (Rogers, 2000). The change can be shown to be

$$\Delta\mathcal{H}(\mathcal{P}) = \mathcal{H}(\mathcal{P}^h) - \mathcal{H}(\mathcal{P}) = \frac{1}{2}\ln\det(\mathbf{Q}^{\mathrm{h}}) - \frac{1}{2}\ln\det(\mathbf{Q}) = \frac{1}{2}\ln\det(\mathbf{Q}^{\mathrm{h}}\,\mathbf{Q}^{-1})\,. \tag{11}$$

The results are summarized in Fig. 8. First we discuss the intramonthly variance spectra shown in Fig. 8a. The overall red spectrum makes it hard to notice that scale-dependent differences, but they are made clear by zooming in the planetary and synoptic scales displayed as an inset panel. It shows a variance reduction of about 6% in the zonal wavenumber $k = 3$ along with the 5% variance increase in $k = 7 - 8$. The blue shading around the variance spectra depicts the 95%-CI obtained through bootstrapping of intramonthly variances. The largest uncertainty is at zonal wavenumbers for the planetary Rossby waves and it shows that the variance reduction at $k = 3$ is within 95%-CI and, therefore, is insignificant. The opposite is found at $k = 7 - 8$, where the change in the intramonthly variance during heat waves is significant.

Figure 8a however does not include the mean zonal state. A more detailed view of the changes in the global intramonthly variance in comparison with entropy is provided in other two panels. The variance reduction (Fig. 8b) and the entropy reduction (Fig. 8c) are qualitatively very similar; they both show a decrease in $k = 3$ along with an increase in $k = 7 - 8$. They also agree about the largest variance and entropy changes being in the zonal mean state with a positive and negative change in the two asymmetrical meridional modes, $n = 4$ and $n = 6$, respectively.

The change in $k = 0$ during Eurasian heat waves can be associated with physical space using the latitudinal structure of the Hough functions[4]. But, perhaps even more insightful is the latitudinal profile of the zonal-mean zonal wind presented in Fig. 9. Figure 9 shows that the maximum zonal-mean zonal wind at 45°N during heat waves is weaker (about 10%) with respect to climatology and slightly shifted (about 1°) northward. The wind maximum is also better confined within the troposphere, with the 10 ms^{-1} isoline at level close 300 hPa compared to level close 200 hPa in climatology. The barotropicity of the midlatitude atmosphere near 45°N, as defined by the VSFs not changing the sign below 250 hPa but still supporting the

[4]The latitudinal profiles of the Hough functions for the Rossby waves with $n = 1 - 4$ are available at https://modes.cen.uni-hamburg.de/Hough.

vertical shear of the mean zonal wind, is decreased during the Eurasian heat waves. Another features of the heat waves are twice stronger zonal-mean zonal winds in higher latitudes between 60°N and 90°N with a peak difference of up to 3 ms^{-1} at 75°N. The dipole shape of the difference in Fig. 9c is in Hough space of Fig. 8b,c seen as an entropy decrease in $n = 4$ and an increase in $n = 6$. Note that Fig. 9 is obtained by filtering to physical space the $\overline{\chi}^0_n$ and that similar filtering for any horizontal or vertical scale of interest is straightforward making the holistic modal-space statistics an attractive global complement to the single-variable, single-level Fourier analysis. We speculate that the enhancement of high latitude $k = 0$ zonal winds is a component of more-persistent double jets over Eurasia during heat waves discussed by Rousi et al. (2022).

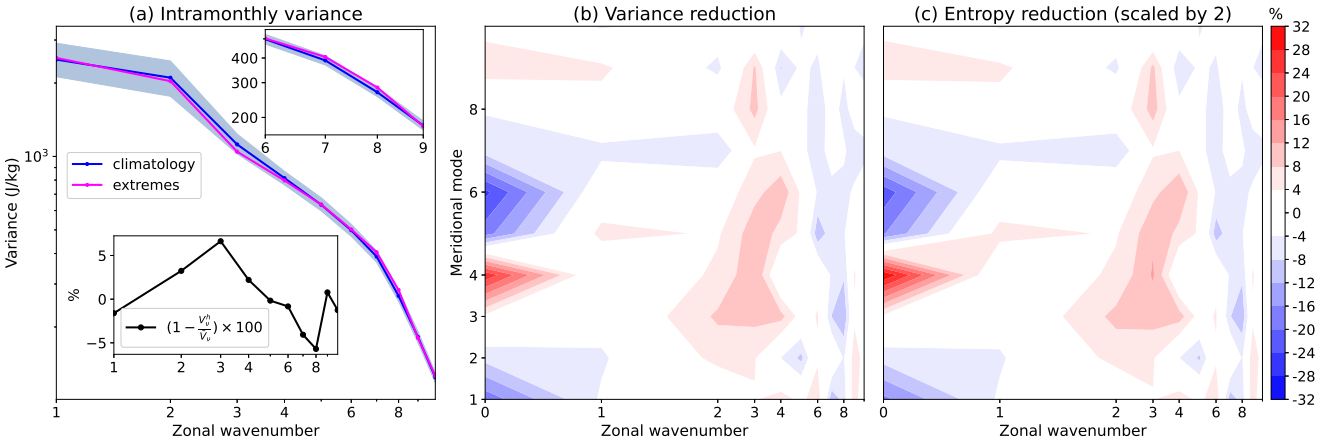

Figure 8. a) Time-averaged intramonthly variance spectra of the Rossby waves for climatology (blue line) and Eurasian heat waves (magenta line). Averaging is performed over a 40-year period 1980-2019, months May-Sep of ERA5. The embedded figure includes (bottom left) the percentage of relative change and (top right) zoomed spectra for $k = 6-9$. The 95%-confidence intervals (blue shading) are obtained through bootstrapping with replacement with 1000 simulations. b) Reduction in the intramonthly variance as a function of the zonal wavenumber starting with the zonal mean state, c) As in b), but the reduction in entropy multiplied by a factor of 2.

4 Conclusions

Extreme events like heat waves at the surface are accompanied by changes in atmospheric circulation across scales. Our study shows that Eurasian heat waves have signatures in the global circulation. The changes in global statistics of the Rossby wave variance are made evident by analyzing the four modern reanalyses: the ERA5, ERA-Interim, JRA-55, and MERRA datasets. Rossby waves are identified by a multivariate projection of the global horizontal winds and geopotential height on the eigensolutions of the linearized primitive equations on the sphere with a basic state at rest (the so-called normal-mode functions). A complete projection basis provides global statistics of Rossby waves as a function of the zonal wavenumber, the meridional mode index and the vertical modes associated with the vertical structure functions that are barotropic within the troposphere.

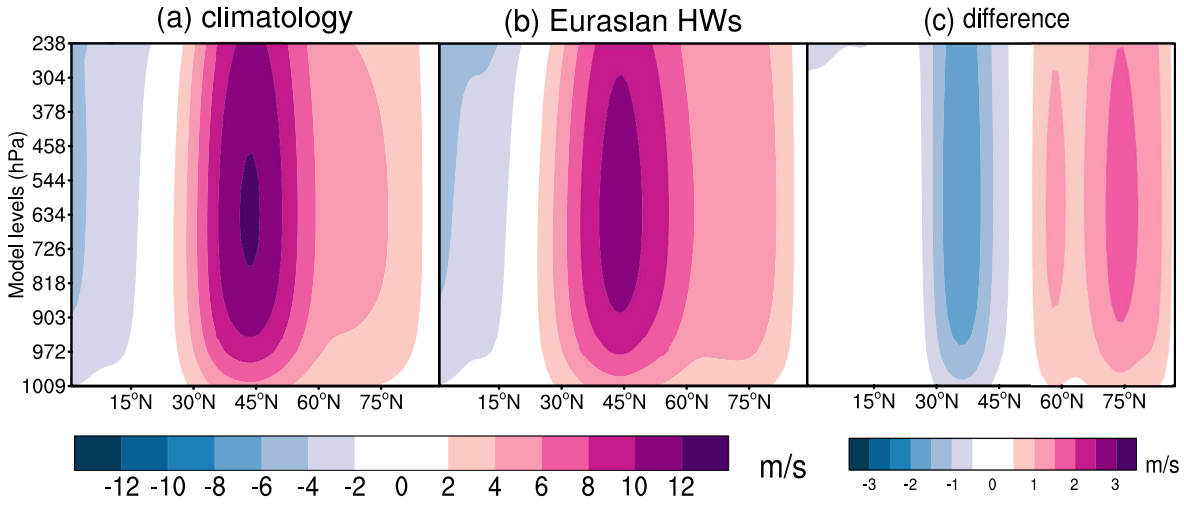

Figure 9. Zonal-mean zonal wind in the northern hemisphere troposphere in 1980-2019, May-Sep ERA5 data. (a) climatology, (b) Eurasian heat waves (HWs) and (c) climatology - heat waves.

The reconstructed physical space picture of the Eurasian heat waves is in agreement with previous studies (Lau and Kim, 2012; Behera et al., 2012; Coumou et al., 2014; Teng and Branstator, 2019). The enhancement of the zonal mean state ($k = 0$) zonal winds in high latitude of the Northern Hemisphere is likely a component of more-persistent double jets over Eurasia during heat waves recently discussed by Rousi et al. (2022). In modal space, this is seen as an increase of around 20% in the intramonthly variance in the zonal mean state asymmetrical Rossby mode with the meridional index 6 along with a similar decrease in the meridional mode 4. In physical space, the dipole-shaped change of the zonal-mean zonal wind is such that the mean westerlies somewhat weaken near their core at 45°N but get twice stronger in high midlatitudes (centred at 75°N). A decreased barotropicity close to 45°N is interpreted as a reduced vertical shear of the mean westerly flow. Future work should couple these findings with the study by Wirth and Polster (2021) on the role of Rossby waves in processes leading to the double jet formation.

The statistical analysis is carried out on the complex time series of the Hough expansion coefficients representing Rossby modes with the troposphere-barotropic structures. We show that the energy distribution of a single mode follows a χ^2-distribution. Statistics of the normalized energy anomalies shows that the zonal mean state ($k = 0$) and the planetary-scale ($k = 1 - 3$) circulation are more skewed than the synoptic and smaller scales, with extended right tails.

During the Eurasian heat waves, the skewness in planetary waves increases while the opposite occurs in the zonal mean flow. The increase in skewness can be linked with a decrease in the number of active degrees of freedom during heat waves. This aligns with the results of Lucarini and Gritsun (2020) which are based on the atmospheric stability during Atlantic blockings. Based on the χ^2-skewness, we estimate a reduction of the active degrees of freedom during Eurasian heat waves of about 25% compared to climatology.

Consistent changes in wavenumebr space are found in the intramonthly variance and entropy. Eurasian heat waves are characterised by a statistically significant increase of about 5% in the intramonthly variance at synoptic scales $k = 7 - 8$, with respect to climatology. This is consistent with increased synoptic activity during blocking (e.g., Shutts, 1983; Yamazaki and Itoh, 2013). In contrast, a reduction of intramonthly variance in $k = 3$ of about 6% is found not to be statistically significant. Future studies with longer datasets, such as climate model outputs are an opportunity for models' validation and larger datasets of extreme events.

Code and data availability. The ERA-Interim and ERA5 reanalysis datasets are available via http://www.ecmwf.int. The MERRA and JRA-55 are available at https://gmao.gsfc.nasa.gov/reanalysis/MERRA and https://jra.kishou.go.jp/JRA-55, respectively. The MODES software can be requested via https://modes.cen.uni-hamburg.de. The time series of the Hough expansion coefficients for the four reanalyses are available upon the request from the authors.

Author contributions. All authors contributed to the study conception and design. IS developed the algorithm, performed the data analysis and wrote a first draft of the manuscript. All authors participated in data interpretation and revised previous versions of the manuscript. All authors read and approved the final manuscript.

Competing interests. The authors declare that the research was conducted in the absence of any commercial or financial relationships that could be construed as a potential conflict of interest.

Disclaimer. TEXT

Acknowledgements. This work was funded by the Deutsche Forschungsgemeinschaft (DFG, German Research Foundation) under Germany's Excellence Strategy – EXC 2037 'CLICCS - Climate, Climatic Change, and Society' (CLICCS, A6) – Project Number: 390683824, contribution to the Center for Earth System Research and Sustainability (CEN) of Universität Hamburg. We thank the former MODES group members at the University of Ljubljana Damjan Jelić and Khalil Karami for the MODES decomposition of the four reanalysis data, to Žiga Zaplotnik for his advice on processing the Hough coefficients in Python, to Qiyun Ma for the algorithm for the heat waves identification and to Frank Sielmann for the variance analysis and technical support. We would also like to thank Valerio Lucarini for the discussion, and to two anonymous reviewers and Editor Dr. Gwendal Riviére for their constructive comments on the manuscript.

References

Barriopedro, D., Fischer, E. M., Luterbacher, J., Trigo, R. M., and García-Herrera, R.: The Hot Summer of 2010: Redrawing the Temperature Record Map of Europe, Science, 332, 220–224, https://doi.org/10.1126/science.1201224, 2011.

Behera, S. K., Ratnam, J. V., Masumoto, Y., and Yamagata, T.: Origin of extreme summers in Europe: the Indo-Pacific connection, Clim. Dyn., 41, 663–676, https://doi.org/10.1007/s00382-012-1524-8, 2012.

Coumou, D., Petoukhov, V., Rahmstorf, S., Petri, S., and Schellnhuber, H. J.: Quasi-resonant circulation regimes and hemispheric synchronization of extreme weather in boreal summer, Proc. Natl. Acad. Sci. U.S.A., 111, 12 331–12 336, https://doi.org/10.1073/pnas.1412797111, 2014.

Dee, D. P., Uppala, S. M., Simmons, A. J., Berrisford, P., Poli, P., Kobayashi, S., Andrae, U., Balmaseda, M. A., Balsamo, G., Bauer, P., Bechtold, P., Beljaars, A. C. M., van de Berg, L., Bidlot, J., Bormann, N., Delsol, C., Dragani, R., Fuentes, M., Geer, A. J., Haimberger, L., Healy, S. B., Hersbach, H., Hólm, E. V., Isaksen, L., Kållberg, P., Köhler, M., Matricardi, M., McNally, A. P., Monge-Sanz, B. M., Morcrette, J.-J., Park, B.-K., Peubey, C., de Rosnay, P., Tavolato, C., Thépaut, J.-N., and Vitart, F.: The ERA-Interim reanalysis: configuration and performance of the data assimilation system, Q. J. R. Meteorol. Soc., 137, 553–597, https://doi.org/10.1002/qj.828, 2011.

Drouard, M. and Woollings, T.: Contrasting mechanisms of summer blocking over western Eurasia, Geophys. Res. Lett., 45, 12–040, https://doi.org/10.1029/2018GL079894, 2018.

Emerton, R., Brimicombe, C., Magnusson, L., Roberts, C., Di Napoli, C., Cloke, H. L., and Pappenberger, F.: Predicting the unprecedented: forecasting the June 2021 Pacific Northwest heatwave, Weather, n/a, https://doi.org/https://doi.org/10.1002/wea.4257, 2022.

Feudale, L. and Shukla, J.: Influence of sea surface temperature on the European heat wave of 2003 summer. Part I: an observational study, Clim. Dyn., 36, 1691–1703, https://doi.org/10.1007/s00382-010-0788-0, 2011.

Fuentes-Franco, R., Koenigk, T., Docquier, D., Graef, F., and Wyser, K.: Exploring the influence of the North Pacific Rossby wave sources on the variability of summer atmospheric circulation and precipitation over the Northern Hemisphere, Clim. Dyn., pp. 1–15, https://doi.org/10.1007/s00382-022-06194-4, 2022.

Galfi, V. M. and Lucarini, V.: Fingerprinting Heatwaves and Cold Spells and Assessing Their Response to Climate Change Using Large Deviation Theory, Phys. Rev. Lett., 127, 058 701, https://doi.org/10.1103/PhysRevLett.127.058701, 2021.

Hersbach, H., Bell, B., Berrisford, P., Hirahara, S., Horányi, A., Muñoz-Sabater, J., Nicolas, J., Peubey, C., Radu, R., Schepers, D., et al.: The ERA5 global reanalysis, Q. J. R. Meteorol. Soc., 146, 1999–2049, https://doi.org/doi.org/10.1002/qj.3803, 2020.

Kasahara, A.: 3D Normal Mode Functions (NMFs) of a Global Baroclinic Atmospheric Model, Modal View Of Atmospheric Variability: Applications Of Normal-Mode Function Decomposition in Weather and Climate Research. N. Žagar and J. Tribbia, Eds., Springer, Mathematics of Planet Earth Series, Vol.8, 2020.

Kautz, L.-A., Martius, O., Pfahl, S., Pinto, J. G., Ramos, A. M., Sousa, P. M., and Woollings, T.: Atmospheric blocking and weather extremes over the Euro-Atlantic sector–a review, Weather Clim. Dynam., 3, 305–336, https://doi.org/10.5194/wcd-3-305-2022, 2022.

Kobayashi, S., Ota, Y., Harada, Y., Ebita, A., Moriya, M., Onoda, H., Onogi, K., Kamahori, H., Kobayashi, C., Endo, H., Miyaoka, K., and K., T.: The JRA-55 reanalysis: General specifications and basic characteristics, J. Meteorol. Soc. Jpn. Ser. II, 93, 5–48, https://doi.org/10.2151/jmsj.2015-001, 2015.

Kornhuber, K., Osprey, S., Coumou, D., Petri, S., Vladimir, P., and Stefan, R. and, G. L.: Extreme weather events in early summer 2018 connected by a recurrent hemispheric wave-7 pattern, Environ. Res. Lett., 14, 054 002, https://doi.org/10.1088/1748-9326/ab13bf, 2019.

Kornhuber, K., Coumou, D., Vogel, E., Lesk, C., Donges, J. F., Lehmann, J., and Horton, R. M.: Amplified Rossby waves enhance risk of concurrent heatwaves in major breadbasket regions, Nat. Clim. Change, 10, 48–53, https://doi.org/10.1038/s41558-019-0637-z, 2020.

Lau, W. K. and Kim, K.-M.: The 2010 Pakistan flood and Russian heat wave: Teleconnection of hydrometeorological extremes, J Hydrometeorol., 13, 392–403, https://doi.org/10.1175/JHM-D-11-016.1, 2012.

Lucarini, V. and Gritsun, A.: A new mathematical framework for atmospheric blocking events, Clim. Dyn., 54, 575–598, https://doi.org/10.1007/s00382-019-05018-2, 2020.

Ma, Q. and Franzke, C. L. E.: The role of transient eddies and diabatic heating in the maintenance of European heat waves: a nonlinear quasi-stationary wave perspective, Clim. Dyn., 56, 2983 – 3002, https://doi.org/10.1007/s00382-021-05628-9, 2021.

Nakamura, N. and Huang, C. S.: Atmospheric blocking as a traffic jam in the jet stream, Science, 361, 42–47, https://doi.org/10.1126/science.aat0721, 2018.

Park, M. and Lee, S.: Relationship between tropical and extratropical diabatic heating and their impact on stationary–transient wave interference, J Atmos Sci, 76, 2617–2633, https://doi.org/10.1175/JAS-D-18-0371.1, 2019.

Perron, M. and Sura, P.: Climatology of non-Gaussian atmospheric statistics, J. Clim., 26, 1063–1083, https://doi.org/10.1175/JCLI-D-11-00504.1, 2013.

Petoukhov, V., Rahmstorf, S., Petri, S., and Schellnhuber, H. J.: Quasiresonant amplification of planetary waves and recent Northern Hemisphere weather extremes, Proc. Natl. Acad. Sci. U.S.A., 110, 5336–5341, https://doi.org/10.1073/pnas.1222000110, 2013.

Ragone, F. and Bouchet, F.: Rare Event Algorithm Study of Extreme Warm Summers and Heatwaves Over Europe, Geophys. Res. Lett.s, 48, https://doi.org/10.1029/2020gl091197, 2021.

Rienecker, M. M., Suarez, M. J., Gelaro, R., Todling, R., Bacmeister, J., Liu, E., Bosilovich, M. G., Schubert, S. D., Takacs, L., Kim, G.-K., Bloom, S., Chen, J., Collins, D., Conaty, A., da Silva, A., Gu, W., Joiner, J., Koster, R. D., Lucchesi, R., Molod, A., Owens, T., Pawson, S., Pegion, P., Redder, C. R., Reichle, R., Robertson, F. R., Ruddick, A. G., Sienkiewicz, M., and Woollen, J.: MERRA: NASA's Modern-Era Retrospective Analysis for Research and Applications, Journal of Climate, 24, 3624 – 3648, https://doi.org/10.1175/JCLI-D-11-00015.1, 2011.

Rogers, C. D.: Inverse Methods for Atmospheric Sounding: Theory and Practice, Series on Atmospheric, Oceanic and Planetary Physics, World Scientific Publ., Singapore, 2000.

Rousi, E., Kornhuber, K., Beobide-Arsuaga, G., Luo, F., and Coumou, D.: Accelerated western European heatwave trends linked to more-persistent double jets over Eurasia, Nat Commun, 13, 3851, https://doi.org/https://doi.org/10.1038/s41467-022-31432-y, 2022.

Schneidereit, A., Schubert, S., Vargin, P., Lunkeit, F., Zhu, X., Peters, D. H., and Fraedrich, K.: Large-scale flow and the long-lasting blocking high over Russia: Summer 2010, Mon Weather Rev., 140, 2967–2981, https://doi.org/10.1175/MWR-D-11-00249.1, 2012.

Screen, J. A. and Simmonds, I.: Amplified mid-latitude planetary waves favour particular regional weather extremes, Nat. Clim. Change, 4, 704–709, https://doi.org/10.1038/nclimate2271, 2014.

Shutts, G.: The propagation of eddies in diffluent jetstreams: Eddy vorticity forcing of 'blocking'flow fields, Q. J. R. Meteorol. Soc., 109, 737–761, https://doi.org/10.1002/qj.49710946204, 1983.

Stefanon, M., D'Andrea, F., and Drobinski, P.: Heatwave classification over Europe and the Mediterranean region, Environ. Res. Lett., 7, 014 023, https://doi.org/10.1088/1748-9326/7/1/014023, 2012.

Sura, P., Newman, M., Penland, C., and Sardeshmukh, P.: Multiplicative noise and non-Gaussianity: A paradigm for atmospheric regimes?, J. Atmos. Sci., 62, 1391–1409, https://doi.org/10.1175/JAS3408.1, 2005.

Teng, H. and Branstator, G.: A zonal wavenumber 3 pattern of Northern Hemisphere wintertime planetary wave variability at high latitudes, J. Clim., 25, 6756–6769, https://doi.org/10.1175/JCLI-D-11-00664.1, 2012.

Teng, H. and Branstator, G.: Amplification of Waveguide Teleconnections in the Boreal Summer, Curr. Clima. Change Rep., 5, 421 – 432, https://doi.org/10.1007/s40641-019-00150-x, 2019.

Trenberth, K. E. and Fasullo, J. T.: Climate extremes and climate change: The Russian heat wave and other climate extremes of 2010, J. Geophys. Res. Atmos., 117, https://doi.org/10.1029/2012JD018020, 2012.

Žagar, N., Kasahara, A., Terasaki, K., Tribbia, J., and Tanaka, H.: Normal-mode function representation of global 3D datasets: open-access software for the atmospheric research community, Geosci. Model Dev., 8, 1169–1195, https://doi.org/https://doi.org/10.5194/gmd-8-1169-2015, 2015.

Wiedenmann, J. M., Lupo, A. R., Mokhov, I. I., and Tikhonova, E. A.: The climatology of blocking anticyclones for the Northern and Southern Hemispheres: Block intensity as a diagnostic, J. Clim., 15, 3459–3473, https://doi.org/10.1175/1520-0442(2002)015<3459:TCOBAF>2.0.CO;2", 2002.

Wilks, D. S.: Statistical methods in the atmospheric sciences, vol. 100 of *International Geophysics*, Academic Press, third edn., http://www.sciencedirect.com/science/bookseries/00746142/100/supp/C, 2011.

Wirth, V. and Polster, C.: The problem of diagnosing jet waveguidability in the presence of large-amplitude eddies, J. Atmos. Sci., 78, 3137–3151, https://doi.org/10.1175/JAS-D-20-0292.1, 2021.

Woollings, T., Barriopedro, D., Methven, J., Son, S.-W., Martius, O., Harvey, B., Sillmann, J., Lupo, A. R., and Seneviratne, S.: Blocking and its response to climate change, Curr. Clima. Change Rep., 4, 287–300, https://doi.org/10.1007/s40641-018-0108-z, 2018.

Xu, P., Wang, L., Liu, Y., Chen, W., and Huang, P.: The record-breaking heat wave of June 2019 in Central Europe, Atmos. Sci. Lett., 21, e964, https://doi.org/10.1002/asl.964, 2020.

Yamazaki, A. and Itoh, H.: Vortex–vortex interactions for the maintenance of blocking. Part I: The selective absorption mechanism and a case study, J. Atmos. Sci., 70, 725–742, https://doi.org/10.1175/JAS-D-11-0295.1, 2013.

Žagar, N., Jelić, D., Blaauw, M., and Bechtold, P.: Energy spectra and inertia–gravity waves in global analyses, J. Atmos. Sci., 74, 2447–2466, https://doi.org/10.1175/JAS-D-16-0341.1, 2017.

Žagar, N., Kosovelj, K., Manzini, E., Horvat, M., and Castanheira, J.: An assessment of scale-dependent variability and bias in global prediction models, Clim. Dyn., 54, 287–306, https://doi.org/10.1007/s00382-019-05001-x, 2019.

Žagar, N., Zaplotnik, Ž., and Karami, K.: Atmospheric subseasonal variability and circulation regimes: spectra, trends, and uncertainties, J. Clim., 33, 9375–9390, https://doi.org/10.1175/JCLI-D-20-0225.1, 2020.

Zhou, Y. and Wu, Z.: Possible impacts of mega-El Niño/Southern Oscillation and Atlantic Multidecadal Oscillation on Eurasian heatwave frequency variability, Q. J. R. Meteorol. Soc., 142, 1647–1661, https://doi.org/10.1002/qj.2759, 2016.